Inorganic Chemistry

pubs.acs.org/IC

Article

Structural Features of a Family of Coumarin–Enamine Fluorescent Chemodosimeters for Ion Pairs

Aaron B. Davis, Michael H. Ihde, Alie M. Busenlehner, Dana L. Davis, Rashid Mia, Jessica Panella, Frank R. Fronczek, Marco Bonizzoni,* and Karl J. Wallace*

Cite This: *Inorg. Chem.* 2021, 60, 14238–14252

Read Online

ACCESS | Metrics & More | Article Recommendations | Supporting Information

ABSTRACT: A family of coumarin–enamine chemodosimeters is evaluated for their potential use as fluorescent molecular probes for multiple analytes [cadmium(II), cobalt(II), copper(II), iron(II), nickel(II), lead(II), and zinc(II)], as their chloride and acetate salts. These fluorophores displayed excellent optical spectroscopic modulation when exposed to ion pairs with different Lewis acidic and basic properties in dimethyl sulfoxide (DMSO). The chemodosimeters were designed to undergo excited-state intramolecular proton transfer (ESIPT), which leads to significant Stokes shifts (ca. 225 nm) and lower-energy fluorescence emission (ca. 575 nm). A more basic anion, e.g., acetate, inhibited the ESIPT mechanism by deprotonation of the enol, producing a binding pocket (N^O$^-$ chelate) that can coordinate to an appropriate metal ion. Coordination of the metal ions enhances the fluorescent intensity via the chelation-enhanced fluorescence emission mechanism. Subjecting the spectroscopic data to linear discriminant analysis provided insights into the source of these systems' markedly different behavior toward ion pairs, despite the subtle structural differences in the organic framework. These compounds are examples of versatile, low-molecular-weight, dual-channel fluorescent sensors for ion-pair recognition. This study paves the way for using these probes as practical components of a sensing array for different metal ions *and* their respective anions.

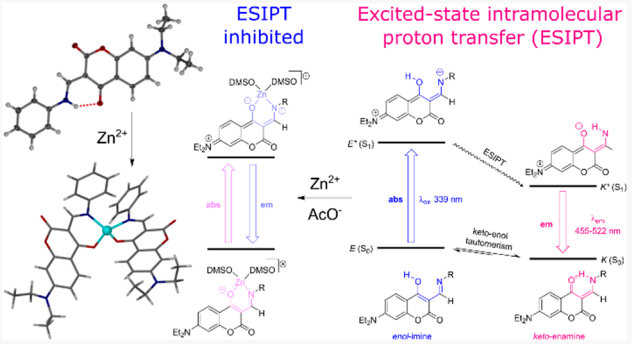

1. INTRODUCTION

Advances in chemical analysis rely heavily on the design of molecular systems that recognize other molecules and respond to their presence with a macroscopic change in their properties (chemosensors).[1] The use of *chemodosimeters*, i.e., compounds that react covalently and *irreversibly* with their targets to form a new species with different properties than the original molecule (e.g., colorimetric or fluorometric signature), is a strategy that is less well explored in the sensor community.[2,3] Chemodosimeters can afford uncommonly high selectivity toward their targets by coupling with chemical cascade methods for response amplification. This approach has had immediate applications for analytical purposes,[4] but it has also proven fruitful further afield, e.g., in the development of novel stimuli-responsive materials.[5]

The choice of a signal transduction mechanism is also critical to the success of chemical-sensing paradigms. Fluorescent molecular probes that utilize the excited-state intramolecular proton transfer (ESIPT) mechanism can display interesting modulation in their optical properties. Moreover, the donor and acceptor involved in the ESIPT form a resonance-assisted hydrogen-bonding (RAHB) interaction. This intramolecular hydrogen bond further delocalizes the electron density in a π-conjugated system.[6] As a result, the ESIPT process leads to a structural change via tautomerization, influencing the molecules' electronic and optical properties. This often leads to large changes in the optical response of these molecules, such as large Stokes shifts in luminescence emission (>200 nm), as well as new absorbance and emission signals. Several fluorophores incorporate the cyclic RAHB motif, including hydroxy- and amino-substituted 2-arylbenzoxazole (HBO),[7,8] 2-arylbenzothiazole (HBT),[9] and anthraquinone (AQ)[10−12] as well as 3-hydroxyflavone (3HF) derivatives[13−15] (Figure 1). In these compounds, the enol tautomer (E) has a distinct UV–vis absorption from the keto tautomer (K). Therefore, it can be separately photoexcited; its excited state E^* readily undergoes proton translocation upon excitation to form the more stable excited state of the keto tautomer (K^*; Scheme 1 and Figure 10). The fluorescence emission of the keto tautomer is accompanied by a large bathochromic shift. The ESIPT mechanism and the photo-

Received: June 9, 2021
Published: September 1, 2021

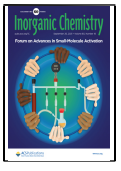

https://doi.org/10.1021/acs.inorgchem.1c01734
Inorg. Chem. 2021, 60, 14238–14252

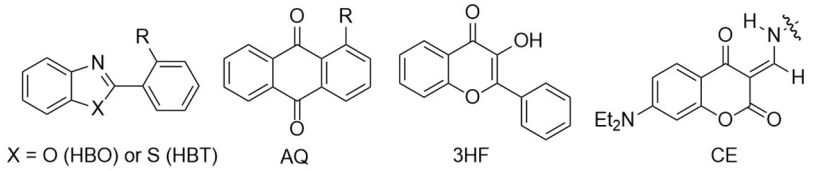

Figure 1. Common functional groups found in fluorescent molecular probes using the ESIPT mechanism (from left to right): HBO or HBT, AQ, 3HF (R = OH or NH), and hydroxycoumarin-based imine−enamine structures.

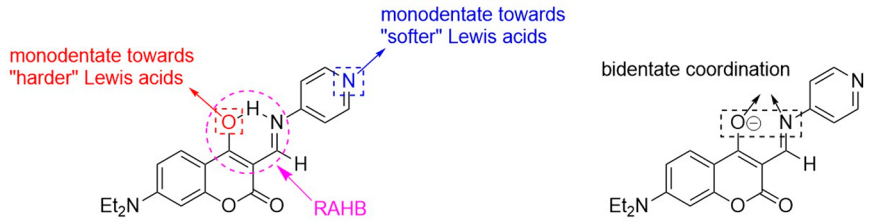

Figure 2. Possible binding sites and coordination modes for metal binding to coumarin−enamine fluorescent probes.

physical properties it imparts to these fluorophores have been extensively studied in solution, as reported in a comprehensive review by Kwon and Park highlighting how the ESIPT mechanism is now utilized in organic optoelectronic materials based on these common small-organic molecules.[16]

Despite the successes of this research area, there are still many challenges that need to be addressed in sensor design. For example, the development of molecular probes to detect structurally similar targets within a family of related analytes is still an open challenge. One strategy relies on a small number of similar yet cross-reactive molecular probes used together as part of a sensor array, as demonstrated by Anslyn et al.,[17] Anzenbacher et al.,[18] Rotello et al.,[19] Kostereli and Severin,[20] and Li and Suslick.[21] Previously, we reported a simple array-sensing ensemble using a family of coumarin−enamine molecular probes that could discriminate 10 divalent metal chloride salts [calcium(II), cadmium(II), cobalt(II), copper(II), iron(II), mercury(II), magnesium(II), nickel(II), lead(II), and zinc(II)].[22] Analysis of the data generated by the array was achieved by pattern recognition tools, such as principal component analysis or linear discriminant analysis (LDA), two statistical data processing methods that are well-established in supramolecular analytical chemistry.[23] Other sensor arrays for metal ions have been reported;[24−26] this approach has also been used to discriminate small organic molecules,[27−29] more complex biomolecules such as nucleotides[30,31] and proteins,[32,33] and biochemical processes, such as aggregation and enzyme activity.[34,35] The nature of the intermolecular interactions between the individual analytes, the structural features of the chemodosimeters and their complexes, and the array components are responsible for their discriminatory analytical power.

2. RESULTS AND DISCUSSION

Here we report a family of structurally similar chemodosimeters that can now simultaneously discriminate between ion pairs. We examined the probes' ESIPT mechanism, coupled with chelation-induced enhancement of the fluorescence emission (CHEF) in the presence of metal(II) salts having a basic counteranion (e.g., acetate).[36,37] Using solid-state techniques and solution studies, which include absorbance and emission experiments, we were able to rationalize the behavior of these coumarin−enamine probes as ligands and chemodosimeters. Moreover, structural changes linked to hydrogen-bond-mediated ESIPT play a pivotal role in the discrimination of ion pairs. The ESIPT is inhibited upon metal-ion binding to give rise to another mechanism (CHEF), providing a distinct fluorescence response.

Sensor Design, Synthesis, and Characterization. We report here on a family of hydroxycoumarin-based fluorophores containing an imine−enamine functional group that can undergo ESIPT and function as molecular probes for colorimetric and fluorescent sensing (Figure 1), a new addition to optical spectroscopic sensing applications.

This work aims to understand the photophysical mechanisms responsible for the optical response of a family of coumarin−enamine dyes in their interaction with metal cations and their counterions; we also used these insights in the development and interpretation of a pattern-based recognition system to differentiate metal-ion pairs. We have previously reported that these chemodosimeters give excellent discrimination of 10 metal(II) chloride salts.[22] In these systems, coordination of the metal can occur via the nitrogen atom in the pyridyl ring system (a borderline Lewis base). However, deprotonation of the enol group by the cation's counterion can produce an additional binding site, forming a bidentate motif (N^O$^-$). The system's affinity for metal cations is therefore mediated not only by the cations' own binding preferences but also by the basicity of the anionic counterion, which can "switch on" a new bidentate binding mode (Figure 2).

Previous work on this system had been limited to chloride salts of metal cations. The chloride ion alone is generally not basic enough to deprotonate the enol proton involved in RAHB to form the N^O$^-$ bidentate binding motif in the molecular probe (Figure 2). Therefore, it was reasonable to assume that, for chloride salts, the coordination of the metal ion occurs at only one of the Lewis basic sites (oxygen or nitrogen atom) in a monodentate fashion. However, deprotonation at the RAHB site with certain metal chlorides can transform the preferred coordination environment to a harder (N^O$^-$) moiety. Such differential behavior among metal cations was previously exploited in our prior work to enhance the discrimination of metal ions. In this work, we extend our studies to metal salts with a more basic counterion, namely, acetate, to investigate the role of the counterion in these interactions. It is known that the acetate anion can

https://doi.org/10.1021/acs.inorgchem.1c01734
Inorg. Chem. 2021, 60, 14238−14252

Scheme 1. Synthesis of the Family of Molecular Probes 3−7[a]

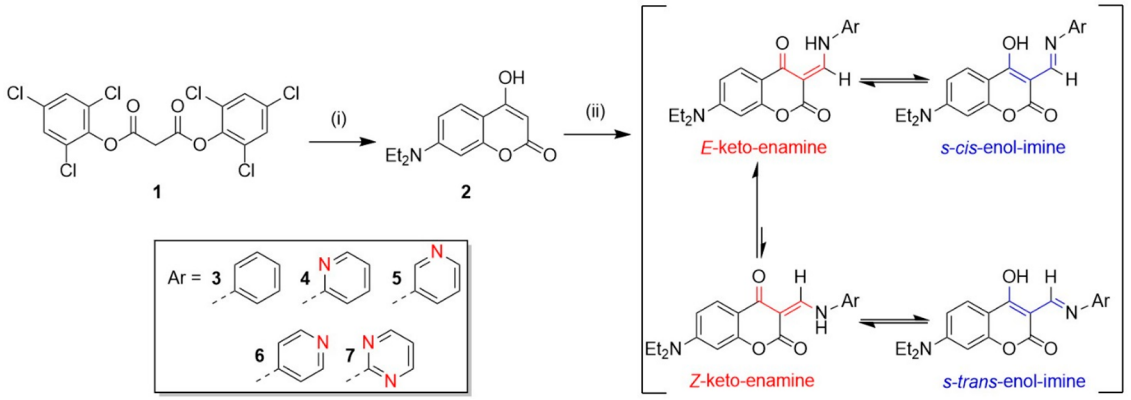

[a](i) 3-(Diethylamino)phenol, toluene Δ; (ii) addition of the appropriate aminopyridine derivative, triethylorthoformate, propan-2-ol, Δ. The possible tautomers (keto vs enol), configurational isomers (*E* vs *Z*), and conformational isomers (s-cis vs s-trans) are shown.

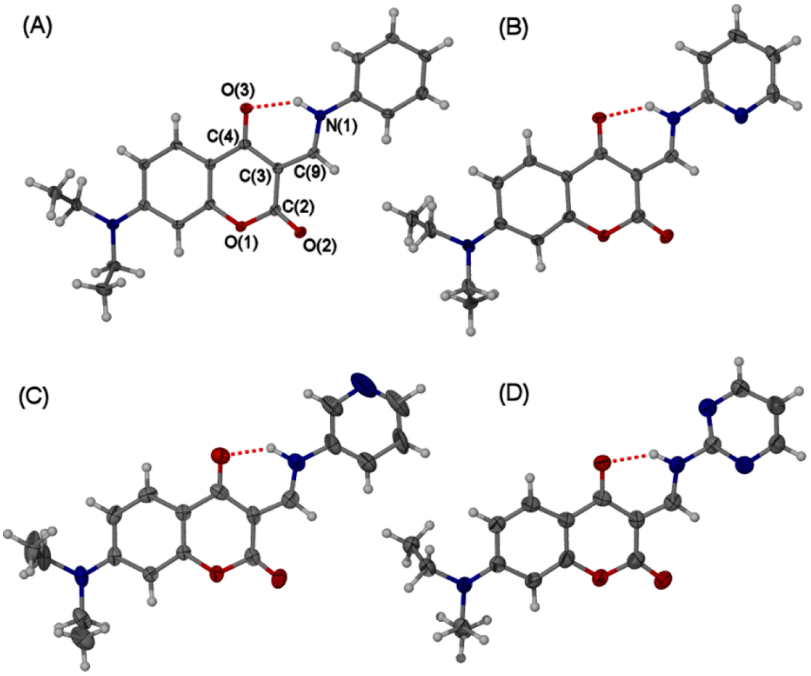

Figure 3. Crystal structures of molecular probes (A) **3**, (B) **4**, (C) **5**, and (D) **7** highlighting selected atom labeling and the displacement ellipsoids at 50% probability. Donor−acceptor distances (Å): intramolecular hydrogen bond N(1)−H···O(3) = 2.621(2), 2.606(3), 2.656(4), and 2.616(4)° for structures **3**−**5** and **7**, respectively.

effectively remove the proton involved in the RAHB system to form the N^O$^-$ chelating motif, thus inhibiting the ESIPT mechanism, but upon coordination of the metal ion, the fluorescence signal is regenerated via CHEF.[36,37]

The synthesis of the molecular probes **3**−**7** is a straightforward three-step process. The commercially available 2,4,6-trichlorophenol and malonic acid are added together to yield bis[2,4,6-(trichlorophenyl)malonate] (known as magic malonate, compound **1**). Compound **1** is then reacted with 3-(diethylamino)phenol to form 7-(diethylamino)-4-hydroxy-coumarin (**2**), a common intermediate for these types of chemodosimeters.[38,39] The coupling of compound **2** with primary amines yields the desired coumarin−enamine chemodosimeters (**3**−**7**) in good yields (greater than 70%). The experimental procedures have been previously reported.[22,40]

The NMR spectra of probes **3**−**7** show that all compounds exist as a mixture of the two *E*/*Z* stereoisomers (Scheme 1).

All crystal structures were deposited to The Cambridge Crystallographic Data Centre: probe **3** (CCDC 2080861), probe **4** (CCDC 2080862), probe **5** (CCDC 2080863), probe **7** (CCDC 2080864), and [Zn(**3**)$_2$] (CCDC 2080948).

To understand the coordination environment of the molecular probe, we prepared two metal coordination compounds, [Zn(**3**)$_2$] and [Zn(**7**)$_2$]. Synthesis of the metal complexes was carried out by adding the desired zinc(II) acetate salt to a boiling methanolic solution of the desired coumarin−enamine compounds (**3** and **7**) and refluxing for 3 h. The solid precipitate was collected and fully characterized to be the pure coordination complexes [Zn(**3**)$_2$] and [Zn(**7**)$_2$].

Solid-State Studies: Crystal Structures of Molecular Probes 3−7. Single-crystal X-ray analysis showed that the

https://doi.org/10.1021/acs.inorgchem.1c01734
Inorg. Chem. 2021, 60, 14238−14252

Table 1. Crystal Data and Structure Refinement for Compounds 3−5, 7, and [Zn(3)$_2$]

	probe **3**	probe **4**	probe **5**	probe **7**	[Zn(**3**)$_2$] complex
formula	$C_{20}H_{20}N_2O_3$	$C_{19}H_{19}N_3O_3$	$C_{19}H_{19}N_3O_3$	$C_{18}H_{18}N_4O_3$	$C_{40}H_{38}N_4O_6Zn$
fw (g mol^{-1})	336.38	337.37	337.37	338.36	736.11
temperature (K)	100	105	100	100	90
wavelength (Å)	1.54184	1.54184	1.54184	1.54184	1.54184
cryst syst	monoclinic	monoclinic	orthorhombic	monoclinic	triclinic
space group	*P*2(1)/*n*	*C*2/*c*	*Pbca*	*C*2/*c*	$P\bar{1}$
a (Å)	5.0907(3)	24.8120(15)	6.2588(3)	24.406(5)	9.2498(3)
b (Å)	22.9118(14)	8.8859(6)	21.8222(12)	8.817(2)	11.6777(4)
c (Å)	14.2623(18)	18.6763(12)	24.0934(14)	18.603(7)	16.1812(5)
α (deg)	90	90	90	90	79.509(2)
β (deg)	92.198(3)	127.172(3)	90	126.777(12)	89.932(2)
γ (deg)	90	90	90	90	77.857(2)
V (Å^3)	1662.3(3)	3281.1(4)	3290.7(3)	3206.2(15)	1678.91(9)
Z	4	8	8	8	2
D_{calcd} (Mg m^{-3})	1.344	1.366	1.362	1.402	1.465
reflns collected	2667	12721	16971	4462	25039
unique reflns	2437	3346	2914	2341	5959
R_{int}	0.037	0.076	0.033	0.089	0.077
unique reflns/restraints/param	2437/0/232	3346/20/248	2914/0/231	2341/4/249	5959/2/470
S	1.12	1.00	1.04	0.99	1.03
R_1 [$F^2 > 2\sigma(F^2)$]	0.043	0.063	0.069	0.075	0.069
wR (F^2)	0.118	0.146	0.197	0.217	0.187

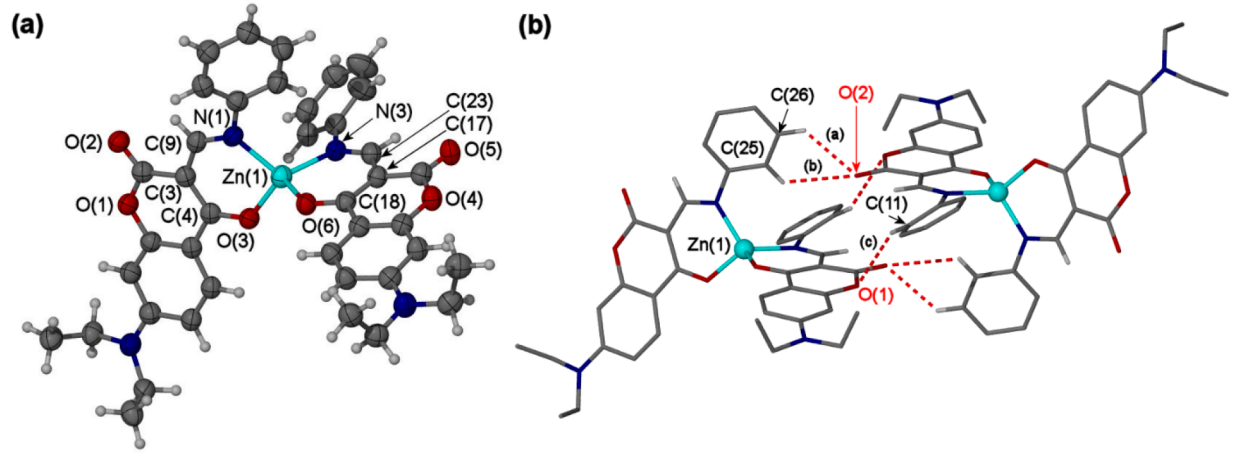

Figure 4. (a) Molecular structure of [Zn(**3**)$_2$], showing the displacement ellipsoids at 50%. (b) Crystal packing of [Zn(**3**)$_2$], with the hydrogen-bonding interactions highlighted. Most of the hydrogen atoms have been removed for clarity; the hydrogen-bonding distances are (a) O(2)^{i}···C(26) = 3.235(5) Å, O(2)^{i}···H(26)C = 2.53 Å; (b) O(2)^{i}···C(25) = 3.412(5) Å, O(2)^{i}···H(25)C = 2.91 Å; (c) O(1)^{i}···C(11) = 3.429(6) Å, O(1)^{i}···H(11)C = 2.59 Å (symmetry code i: $-x + 1, -y + 1, -z$).

four chemodosimeters **3**−**5** and **7** adopt their thermodynamically stable *E*-keto enamine isomer (Figure 3 and Table 1). The X-ray structure of compound **6** has been previously published.[40] Crystals for all four compounds were grown from the slow evaporation of a concentrated solution of dimethyl sulfoxide (DMSO). All of the coumarin−enamine ligands are essentially planar, possessing a strong intramolecular hydrogen-bonding interaction in O(3)···H−N(1), exhibiting the S(6) ring motif, namely, a RAHB motif, yielding a continuous pseudoring system throughout the molecule, and stabilizing the planarity of the molecule (Figure 3), which explains the optical properties of these chemosensors (see the Optical Spectroscopic Studies of 3−7 section).

The molecular structures show interesting supramolecular features. Compound **3** exhibits two sets of bifurcated hydrogen-bonding interactions CH···O between C(11′)H and C(9)H of the *E*-keto isomer and the oxygen atom O(2) of an inversion-related molecule that is anti in orientation (Figure S1). The crystal packing shows that the molecule forms a *π*-stacking offset interaction with a ring separation of 3.61 Å. There is also evidence that the crystal packing is further stabilized by an edge-to-face CH···*π* interaction between two molecules separated by 3.44 Å (Figure S2). The overall packing motif for probe **3** can be described as a pseudo-*γ*-structure (Figure S3).

Conversely, probe **4** does not show the two sets of bifurcated networks observed in probe **3**. However, a *π*-stacking interaction (3.63 Å) is observed between the electron-rich pyridine unit of one molecule with the electron-deficient ring system of another molecule's coumarin backbone in an inverted fashion (Figure S4). The introduction of the pyridine group significantly changes the supramolecular architecture, in

https://doi.org/10.1021/acs.inorgchem.1c01734
Inorg. Chem. 2021, 60, 14238−14252

which a ladderlike structure is formed (Figure S5). The overall packing motif is facilitated by weak nonclassical hydrogen-bonding interactions between the nitrogen atom in the pyridine unit and the CH group on the coumarin backbone binding to a CH on the ethyl group of a neighboring molecule (Figure S6), reminiscent of the classical γ-structure seen in other aromatic systems.[41] Interestingly, probe **5** does not show any evidence of π-stacking interactions. Instead, the overall structure is stabilized by an array of weak hydrogen-bonding motifs between adjacent molecules in a zipper-type fashion (Figures S7−S9). Finally, the crystal structure of probe **7** is very similar to that of probe **4** presumably because of the pyrimidine moiety containing two nitrogen atoms, one of which occupies the same ortho position as probe **4**. The π-stacking distances between two adjacent molecules are modestly shorter, 3.58 Å (probe **7**) compared to 3.61 Å (probe **4**). However, the packing motifs are virtually identical with those of probe **4** (Figures S10−S12).

Crystal Structure of [Zn(3)$_2$] Complex. The zinc ion can adopt an array of geometries, with a preference for tetrahedral structures but also including square-pyramidal, trigonal-bipyramidal, and octahedral structures, and a plethora of pseudogeometries too.[42]

X-ray-quality crystals of [Zn(**3**)$_2$] were obtained by the slow evaporation of a concentrated solution of DMSO over several days. The molecular structure of [Zn(**3**)$_2$] is shown in Figure 4. Two coumarin−enamine ligands are coordinated to the zinc(II) ion center in a chelating fashion by the oxygen and nitrogen atoms via the keto−enamine functional group. This is indicated by the bond lengths of the short C═O bond of the dione [O(3)−C(4)] and the C═N bond of the imine moiety [N(1)−C(9)], which are 1.280(5) and 1.310(5) Å, respectively, for one of the ligands; the bond lengths for the second ligand are essentially equivalent. In fact, there are only minor differences in the bond lengths and bond angles of the two monoanionic bidentate coumarin−enamine ligands. The Zn^{II}−O and Zn^{II}−N bonds produce a stable six-membered chelating motif, which is favorable for smaller metal ions.[43] The lengths of the Zn^{II}−O bonds Zn(1)−O(3) and Zn(1)−O(6) [1.919(3) and 1.932(3) Å, respectively] and the Zn^{II}−N bonds for the imine moiety, Zn(1)−N(1) and Zn(1)−N(3) [1.998(3) and 1.981(3) Å, respectively], are in excellent agreement with similar chelating motifs.[44−46] The zinc(II) ion's molecular geometry is distorted tetrahedral, with all bond angles around the zinc(II) center ranging between 109.4 and 122.0°. As discussed above, the crystal structure of compound **3** showed a π-stacking arrangement due to the organic framework's planarity. Interestingly, upon the zinc(II) metal ion's coordination, the ligand's planarity is lost, and the aniline group is twisted out-of-plane by approximately 30°. This twist is stabilized by a single hydrogen-bonding interaction between C(11)H from the ligand of one coordination molecule and the oxygen atom on an adjacent molecule, shown in Figure 4b. Because of the pseudotetrahedral geometry around the metal center, there is no evidence of π−π-stacking interactions in the crystal packing of the metal complex. Moreover, these compounds are neutral, with no counterion or coordinating solvent to bind to the metal centers.

We made numerous efforts to grow crystals of the other coordination compounds to no avail. This is because the nitrogen atoms in the aromatic ring of these ligands increase the hydrolysis (see NMR discussion), leading to degradation of the coordination complexes in the weeks necessary for crystals to grow. However, this was not an issue with the spectroscopic studies, which are completed within hours rather than weeks. In lieu of crystal structure determination, we carried out an IR study to help validate the binding mode of zinc(II) ions within the enamino−ketonate (N^O$^-$) motif. The IR study was conducted on free ligands **3**, **6**, and **7** and for the corresponding coordination complexes [Zn(X)$_2$], where X = **3**, **6**, and **7**, as a solid using an attenuated-total-reflectance IR (Figures S13−S15 and Table S1). Overall, a comparison of the IR spectra of the free ligands and zinc complexes for ligands **6** and **7** with those obtained with ligand **3** supports our hypothesis that the binding motifs observed in the crystal structure of [Zn(**3**)$_2$] can be extended to the complexes of the other ligands as well.

Solution Studies. *NMR Studies.* Both the coordination compounds [Zn(X)$_2$], where X = **3** and **7**, and the corresponding free enamine ligands (compounds **3** and **7**) were extensively studied using one-dimensional (1D) ^{1}H and ^{13}C NMR and two-dimensional (2D) NMR (HSQC and HMBC). The numbering scheme of the ligands **3** and **7** and their respective coordination complexes are shown in Figures S16, S25, S31, and S40, respectively. Full spectra are shown in Figures S17−S24, S26−S30, S32−S39, and S41−S45 and Tables S2−S5. Compounds **3** and **7** exist as two stereoisomers (*E* and *Z*); the tautomers were not observed separately in solution (Scheme 1). The *E* and *Z* isomers are distinguishable in the ^{1}H NMR spectrum due to distinct signals generated by the NH functional groups of the *E*- and *Z*-keto enamine. These two signals appear in the region of 13−14 ppm for *E*-keto and 11−12 ppm for *Z*-keto, depending on the ligand. The ^{13}C NMR spectrum proved to be more complicated to assign for the free ligands. ^{13}C attached proton test (APT) experiments were carried out to unambiguously give the different chemical shifts of the carbon atoms (Figures S19−S21 for probe **3** and Figure S28 for probe **7**).

To obtain a chelating motif to coordinate to the metal ion, the hydrogen atom that participates in the RAHB ring system must be removed to form the β-diketonate. In our previous work,[40] we had identified stark differences in behavior among different anions acting as the metals' counterions. For instance, we observed that small, highly charged anions (hard Lewis bases) were able to abstract a proton attached to a highly electronegative atom. On the other hand, a stronger nucleophile such as a cyanide ion, would prefer to add to these structures through a Michael addition. In our previous metal-ion-sensing study using these probes,[22] we did not systematically investigate these effects, settling on using a noninterfering anion (i.e., chloride) instead. In the present work, however, we investigate the impact of the anion in generating the chelating motif described above. The first approach was to investigate whether the relevant proton can be abstracted with an appropriate anion. Initially, we prepared an NMR tube containing coumarin−enamine ligand **6** and 1.3 equiv of either tetra-*n*-butylammonium fluoride (TBAF) or $TBACH_3CO_2$ (Figures S46−S48). We reran the ^{1}H NMR, and within 30 min, it was clear that another compound was being formed. To ascertain the nature of this new compound, we chose to investigate whether the fluoride and acetate ions interacted with the coumarin molecule through hydrogen bonding or proton abstraction. Compound **7** was analyzed by ^{1}H NMR titration at room temperature in $CDCl_3$. Aliquots of TBAF were added to compound **7**; there was little evidence of any hydrogen-bonding interactions. However, the two enamine

https://doi.org/10.1021/acs.inorgchem.1c01734
Inorg. Chem. 2021, 60, 14238−14252

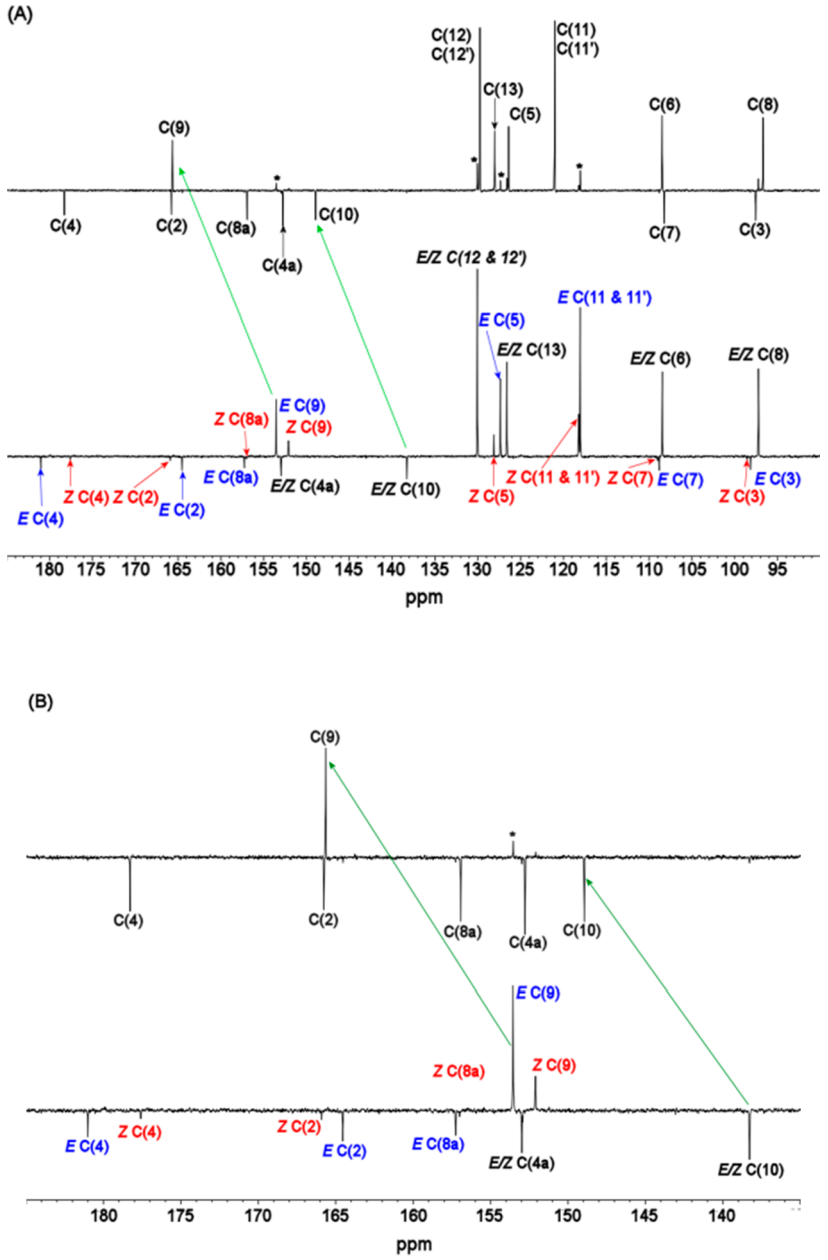

Figure 5. Stacking plot of the ^{13}C NMR-APT in $CHCl_3$-*d*; (A) 95−180 ppm region; (B) 135−185 ppm region. (bottom) Probe **3**. (top) Isolated coordination complex $[Zn(\mathbf{3})_2]$ (*) residual probe **3**.

NH signals at 13.5 and 11.7 ppm disappeared. Upon the addition of 1 equiv of TBAF, an aldehydic proton signal was observed at 10.4 ppm, caused by hydrolysis of the enamine functionality. The two products of the postulated hydrolysis, **2** and 4-aminopyridine, were both identified in the ^1H NMR spectrum (Figure S46). Because fluoride was found to induce side reactions instead of deprotonation, it was abandoned, and we turned our attention to the acetate ion.

On the other hand, when aliquots of $TBACH_3CO_2$ were titrated into probe **7** (Figure S47), hydrolysis was reduced to a minimum (<5%). Therefore, we chose to use the metal acetate salts in our ion-pair studies in DMSO for two reasons: first, metal acetate salts have greater solubility than metal fluorides; second, the acetate ion has been shown to be less basic than fluoride in DMSO (pK_a = 12.7 vs 15 for AcOH[47] and HF,[48] respectively). Furthermore, the presence of a hydrolyzed product was further confirmed because, in the case of probe **7**, we were able to isolate and characterize its octahedral zinc(II) complex using single-crystal X-ray crystallography.[49] The solid-state structure of the hydrolyzed compound showed that a zinc(II) ion was coordinated in a bidentate fashion between the two carbonyl groups. A proposed mechanism explaining the hydrolysis is shown in the Supporting Information (SI) and Scheme 1. Interestingly, compound **3** did not show appreciable hydrolysis, presumably because of the lack of nitrogen atoms in the ring system.[50]

The ^1H and ^{13}C NMR assignments of the $[Zn(\mathbf{3})_2]$ and $[Zn(\mathbf{7})_2]$ coordination compounds were less challenging to interpret. In both cases, one major species is seen. The crystal structure for $[Zn(\mathbf{3})_2]$ shows that compound **3** coordinates to the zinc(II) ion in a pseudo-T_d geometry. The ^1H NMR spectrum of $[Zn(\mathbf{3})_2]$ shows modest chemical shifts between

https://doi.org/10.1021/acs.inorgchem.1c01734
Inorg. Chem. 2021, 60, 14238−14252

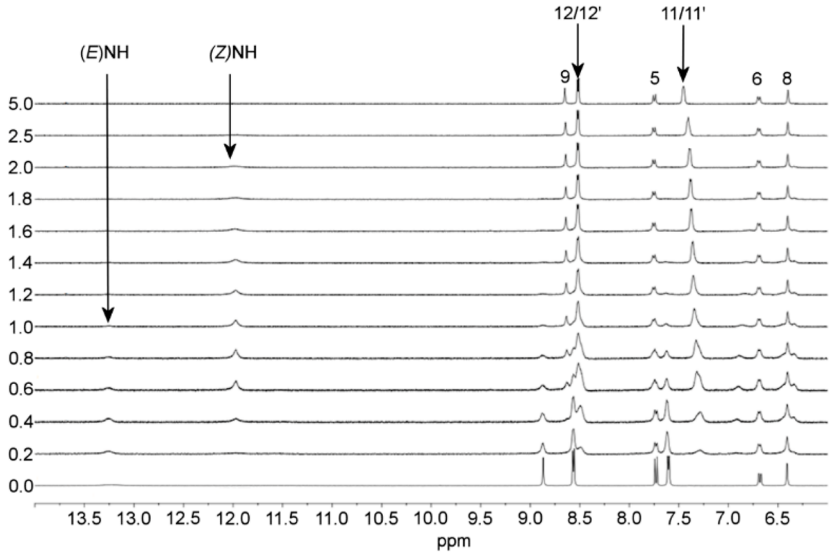

Figure 6. ^{1}H NMR (partial spectra) titration of compound **6** and $Zn(CH_3CO_2)$ in DMSO-d_6.

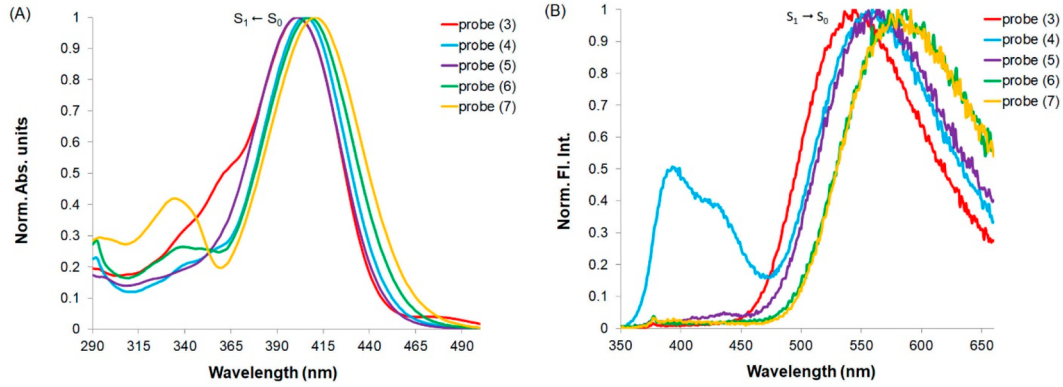

Figure 7. Normalized absorption (A) and emission (B) spectra of probes **3**−**7** in DMSO (16 μM).

the free compound **3** and the coordination complex. The most significant change in the ^{1}H NMR spectrum is the loss of the NH signal. However, the chemical environment of the carbon atoms that make up the chelating motif of ligand **3** showed significant changes in the ^{13}C NMR spectrum upon zinc(II) coordination and, in particular, in the ^{13}C APT experiment, in which the sp^2-hybridized C(9)H showed a positive signal seen at 153.6 ppm in the ligand, whereas this carbon signal shifted downfield to 165.7 ppm in the zinc(II) complex ($\Delta\delta$ 12.1 ppm). Carbon 10, seen as a negative signal at 138.7 ppm in the ^{13}C ATP experiment for the free ligand, shifted to 148.9 ($\Delta\delta$ 10.2 ppm) in the zinc(II) complex. Modest chemical shifts were observed for the other carbon atoms in the six-membered ring system, as shown in Figure 5. The same trend was seen for compound **7** and $[Zn(\mathbf{7})_2]$ (Figures S28 and S43, respectively).

^{1}H NMR Titration with $Zn(CH_3CO_2)_2$. ^{1}H NMR titrations were used to investigate the ion-pair binding ability of compounds **6** and **7** to $Zn(CH_3CO_2)_2$ at room temperature in DMSO-d_6. Aliquots of the metal salt were added to a 15 μM solution of compound **6** or **7**. During the NMR titrations, there was no evidence of hydrolysis, as indicated by the absence of a formyl proton signal and of any free amine being formed in the solution, as shown in Figure 6 for compound **6**.

Interestingly, upon the addition of $Zn(OAc)_2$ to probe **6**, a gradual disappearance of the NH and C(9)H signals was observed. After the addition of 1 equiv of the metal salt, there is evidence that two species exist in solution. The first is the free ligand; the second is a 1:1 zinc(II)/**6** complex. This is seen by a new signal appearing at 8.65 ppm assigned to the C(9)H imine proton. An analogous titration was carried out with compound **7** (Figure S49); again, there was no evidence of hydrolysis; upon the addition of $Zn(CH_3CO_2)_2$, two distinct sets of signals were observed, for the free ligand and $[Zn(\mathbf{7})_2]$. Unfortunately, because the proton signals shifted only modestly upon binding, it was not possible to obtain binding constants using NMR spectroscopy.

Optical Spectroscopic Studies of 3−7. The NMR studies showed that both the (*E*)- and (*Z*)-keto-enamine stereoisomers are present in the solution, but it was unable to resolve the keto-enamine and enol-imine tautomers for each stereoisomers, as the equilibrium between the two tautomers of each stereoisomer is faster than the NMR time scale under these conditions. We then turned to studying the UV−vis absorption properties for all molecular probes (compounds **3**−**7**) in a 100% DSMO solution (16 μM). The UV−vis absorption studies showed a strong absorption band at approximately 400 nm, which was assigned to the keto tautomer, and a weaker but distinctive band or a shoulder

https://doi.org/10.1021/acs.inorgchem.1c01734
Inorg. Chem. 2021, 60, 14238−14252

Table 2. Optical Properties of Molecular Probes 3−7 in DMSO (16 μM), Where Values for the Enol Tautomer Are in Parentheses

molecular probe	ϕ_f yield[a]	λ_{abs}(nm)	$\lambda_{keto\ em}$(nm)	λ_{em}(nm) CHEF	Stokes shift $\lambda_{(enol)\ abs\ at\ 339\ nm}-\lambda_{keto\ em}$
3	0.70	(339, 361), 401	546	455	207
4	0.78	(339,357), 406	560	503	221
5	0.65	(323, 339), 403	564	503	225
6	0.59	(339), 408	581	521	242
7	0.79	(339), 411	580	522	241

[a]Anthracene and quinine sulfate were used as standards.

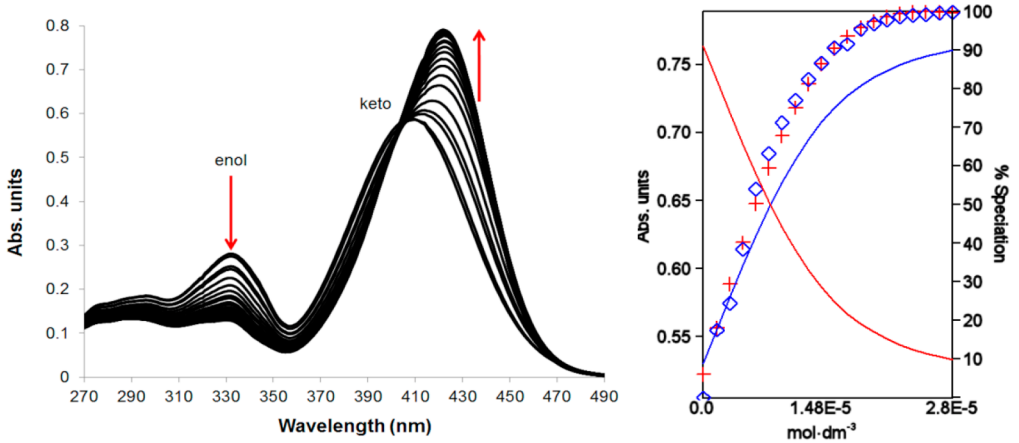

Figure 8. (Left) Absorbance spectra of probe **7** upon the incremental addition of a 1.54 μM stock solution (0.1 up to 2.0 equiv) of $Zn(CH_3CO_2)_2$ in DMSO. (Right) Nonlinear least-squares fit isotherm (blue diamonds and red crosses correspond to the experimental and calculated data, respectively). Solid lines show the percent speciation formed of a free ligand (red) versus complex (blue) during the titration.

between 323 and 361 nm, assigned to the enol form (Figure 7A and Table 2). The electronic properties of keto versus enol tautomers are different enough to show up as distinct bands in the absorption spectrum; furthermore, the two tautomers could be separated here because of the much faster time scale of the electronic absorption experiments. In contrast to the NMR results, we did not detect an appreciable difference in the optical spectra of the *E* and *Z* stereoisomers, presumably because their electronic properties are similar and so are their absorption characteristics. The absorption and steady-state emission spectra of molecular probes **3**−**7** in DMSO are shown in Figures 7 and S50. The absorption spectra are dominated by the keto absorption band, in excellent agreement with the solid-state structure, wherein all of the molecular probes were found in the thermodynamically stable keto isomer.

The quantum yields obtained for compounds **3**−**7** in DMSO are reported in Table 2. Reference compounds used in the study are anthracene and quinine sulfate (Figure S51). The φ_f yields are approximately equal, which is unsurprising because the organic frameworks are similar. The molecular probe's planarity is stabilized by a robust intramolecular hydrogen-bonding interaction, forming a pseudo ring system. The differences in the quantum yields can be attributed to the positions of the nitrogen atoms in the pyridyl ring.

We have previously studied the photophysical properties of molecular probe **6** in detail.[40] Because we had used DMSO as a solvent in our previous studies, we did the same here for consistency. In this work, the absorption spectra for compounds **3**−**7** show a subtle bathochromic shift as the number of nitrogen atoms in the aromatic moiety increases; the incorporation of the nitrogen atoms upon going from benzene (probe **3**) to pyridine (**4**−**6**) to pyrimidine (**7**) seems to slightly stabilize the electronic structure of the excited-state enol moiety.

When the fluorescence emission of the metal-free probes in DMSO when excited at 339 nm (enol band) is studied, a dominant emission band is seen between 532 and 573 nm (Table 2), with a Stokes shift between 207 and 241 nm, assigned to the $S_0 \leftarrow S_1$ transition. This characteristically large Stokes shift is caused by the intramolecular proton transfer that transforms the excited-state enol tautomer into a ground-state keto one. This is in excellent agreement with previously published work by Chen and Hu, who showed that replacing the hydrogen atom on the enol oxygen atom with a methyl functional group significantly reduces the Stokes shift of the emission band.[51]

The binding affinity of compounds **3**−**7** with an array of metal ions as their acetate salts was then studied by UV−vis spectroscopy in DMSO. We screened a series of metal ions by preparing a solution of each chemoreactor in DMSO and adding 2 equiv of metal ion [silver(I), sodium(I), calcium(II), cadmium(II), cobalt(II), copper(II), iron(II), mercury(II), manganese(II), nickel(II), lead(II), and zinc(II)]. In most cases, coordination of the chemodosimeter only produced modest spectroscopic shifts for compounds **3**−**5** (Figure S53). Two metal ions [cobalt(II) and zinc(II)] shifted the absorption maximum in the bathochromic direction. On the other hand, compounds **6** and **7** showed the greatest shifts upon the addition of cadmium(II) and zinc(II) acetate, and a detailed binding study was carried out on probe **7** with $Zn(CH_3CO_2)_2$ in DMSO. Probe **7** showed two distinctive broad bands at 339 and 411 nm in its absorption spectrum (vide supra). Upon the addition of aliquots of zinc(II) ions, the

https://doi.org/10.1021/acs.inorgchem.1c01734
Inorg. Chem. 2021, 60, 14238−14252

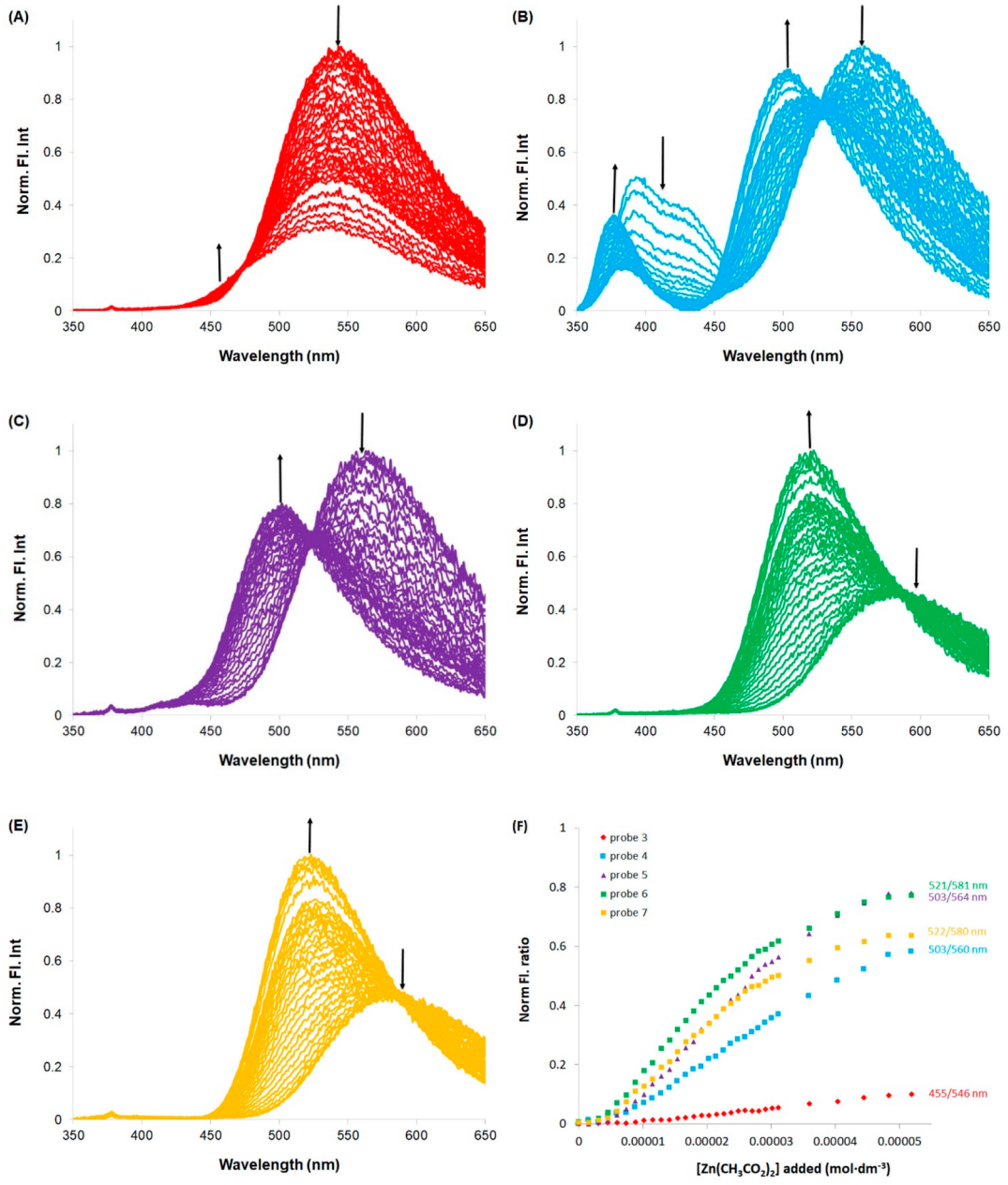

Figure 9. Molecular probes (16 μM) plus aliquots of $Zn(CH_3CO_2)_2$ acetate up to 5 equiv in DMSO [$\lambda_{ex(enol)}$ = 339 nm]: (A) **3**, (B) **4**, (C) **5**, (D) **6**, (E) and **7** (F) isotherms for each molecular probe.

band at 339 nm (enol tautomer) decreased in intensity, and a new more intense red-shifted band appeared at 421 nm through an isosbestic point (407 nm; Figure 8). The binding isotherm could be fitted to a 1:2 (M/L) binding model with log β_{12} = 10.7 ± 0.3 using the nonlinear least-squares fitting program *HypSpec*.[52]

Because different stoichiometries can form in solution, the existence of the 1:1 complex was confirmed by mass spectrometry, whereby a solution containing equimolar amounts of probe **7** and $ZnCl_2$ was allowed to equilibrate for 10 min and directly injected into the mass spectrometer. The negative-ion-mode electrospray ionization mass spectrometry spectra of this mixture shows the expected peaks at m/z 471, 473, and 475 attributed to the $[Zn(7)Cl_2]^-$ anion, with excellent agreement with the expected isotopic distribution (Figure S61). Fragmentation of the m/z 471 peak shows that the coordination compound fragments to the ligand **7** seen at m/z 337 mass units (Figure S62). Because the probe/metal ratio was deliberately set to 1:1 in this solution, there was no evidence of the 2:1 complex that had been observed in the UV−vis titration.

Additionally, a simple test was carried out on the probe alone, whereby 2 equiv of ZnX_2 (X = Br^-, Cl^-, NO_3^-, $CH_3CO_2^-$, ClO_4^-) was added to probes **4** and **7** (Figure S52). Among the salts tested, $Zn(CH_3CO_2)_2$ caused by far the largest change of the probe's emission intensity, suggesting that both the cation and anion in the ion pair are necessary to produce the greatest desired optical responses.

Fluorescence Studies. The steady-state emission of compounds **3**−**7** exhibits a single broad band, with an anomalously long emission tail around 580 nm in DMSO when excited at the enol tautomer absorption band at 339 nm.

https://doi.org/10.1021/acs.inorgchem.1c01734
Inorg. Chem. 2021, 60, 14238−14252

This long tail is due to the proton back-transfer from the enol excited state to the keto tautomer in the ground state, indicative of the ESIPT mechanism and in agreement with the published work.[53] Additionally, only a single emission band is observed, corresponding to the emission of the keto tautomer; no emission can be assigned to the excited state of the enol tautomer, suggesting an ultrafast rate of the ESIPT mechanism. Indeed, this process has previously been calculated to occur on the femtosecond time scale.[51]

Among the metal acetate salts tested, the zinc(II) ion produced the greatest changes in the emission spectra, as seen in the absorbance experiment discussed above. Thus, the photophysical and binding behaviors of compounds **3**−**7** toward zinc(II) acetate were studied in DMSO. Upon excitation at 339 nm (enol tautomer), a broad emission band assigned to the keto* tautomer was seen between 580 and 600 nm. Upon the addition of aliquots of $Zn(CH_3CO_2)_2$ to the molecular probes, the ESIPT emission band (originating from the keto tautomer) decreased in intensity, with a concomitant increase of a new band between 455 and 522 nm (Figure 9). This hypsochromic shift indicated an inhibition of the ESIPT mechanism by proton abstraction via the acetate anion and zinc(II) coordination; the new band was therefore assigned to the direct emission from the enol tautomer. All probes exhibited a significant blue shift upon zinc(II) coordination, indicating strong inhibition of the ESIPT mechanism (Figure 9).

The fluorescence enhancement observed in Figure 9 can be attributed to a CHEF mechanism. To support this, the fluorescence emission spectra of all molecular probes were obtained in the presence of the same series of metal ions used in the UV−vis absorption studies [silver(I), sodium(I), calcium(II), cadmium(II), cobalt(II), copper(II), iron(II), mercury(II), manganese(II), nickel(II), lead(II), and zinc(II)] but this time exciting directly at the keto absorption band (408 nm) to bypass the ESIPT mechanism. Upon the addition of 2 equiv of the metal salt, the emission of the keto excited state was quenched (Figure S54). When zinc(II) and cadmium(II) salts were added, they again produced the greatest changes in the emission spectra: photophysical studies and the binding behavior of compounds **3**−**7** toward these two metal(II) acetates carried out in DMSO with excitation at 408 nm are included in Figures S55 and S57. This behavior is a traditional receptor−analyte mechanism. The emission enhancement was most evident for the zinc(II) ions regardless of the choice of the excitation wavelength (i.e., either 339 or 408 nm). This can be explained by the extra π-electron delocalization of the ligand and also by the enhanced rigidity of the fluorophores as a result of metal coordination. The binding affinity in DMSO between the molecular probes and zinc(II) was determined by nonlinear least-squares analysis (Figures S56 and S58). For the experimental data to fit the binding model, both 1:1 and 2:1 ($probe_2$/metal) species had to be included (Table 3). Because a fluorescence enhancement is seen at approximately 500 nm upon the addition of $Zn(CH_3CO_2)_2$, we used fluorescence spectroscopy to determine the limit of detection (LOD) of zinc(II) ions upon the addition of probes **5** and **7**. The LOD was determined by least-squares linear regression. The confidence limit of the slope is defined as $B \pm tSB$, where t is the Student's t value taken from the desired confidence level and $n - 2$ degrees of freedom (df); here a 95% confidence level (t value 1.89 for df = 7 and t value 2.015 for df = 5 for compounds **5** and **7** respectively) was adopted (Figures S59 and S60). It is accepted that the LOD is the analyte concentration, giving a signal equal to that of the blank signal plus three standard deviations from the blank, i.e., $y = yB + 3SB$. The LOD values were calculated to be 0.15 ppm for probe **5** (obtained as the average of two measurements, λ_{ext} at 339 and 408 nm) and 0.17 ppm for compound **7**.

Table 3. Binding Constants Obtained Using the Nonlinear Regression Program *HypSpec*.

	zinc(II)		cadmium(II)	
molecular probe	log K_{11}	log K_{21}	log K_{11}	log K_{21}
3	3.55 ± 0.14	*a*	4.96 ± 0.01	*a*
4	4.89 ± 0.15	5.53 ± 0.15	4.53 ± 0.01	5.64 ± 0.03
5	5.34 ± 0.11	*a*	5.32 ± 0.1	5.25 ± 0.02
6	5.55 ± 0.32	4.02[b]	4.86 ± 0.01	4.97 ± 0.03
7	5.72 ± 0.08	4.82[b]	4.97 ± 0.01	5.65 ± 0.01

[a]Not needed in the model. [b]Errors are 10−15%; log K_{21} corresponds to the $Probe_2$·Zn species.

On the basis of the spectroscopic data discussed above, a simplified energy-level diagram can be drawn, illustrating the structures and relative energies of the electronic states of these ligands and complexes (Figure 10) responsible for their photophysical properties. The higher-energy enol tautomer (E) can be photoexcited around 339 nm. The enol's excited state (E*) undergoes fast intramolecular proton transfer (ESIPT) to produce the keto form in its excited state (K*); the observed fluorescence emission of the free ligands stems from deexcitation of this K* excited state: the corresponding emission from the keto tautomer shows a significant bathochromic shift. Upon the addition of the metal salt, the anion in the salt induces ligand deprotonation, thus preventing the ESIPT process. Therefore, upon coordination of the metal to the deprotonated ligand, the emission wavelength shifts toward blue and increases in intensity, with the latter increase being due to chelation enhancement, as discussed above.

Multivariate Study of Metal-Ion Pairs: Acetate versus Chloride. In the work described above, metal(II) acetate salts displayed a significantly different colorimetric and fluorescence response than the metal(II) chlorides studied in our previous work.[22] Nevertheless, obtaining detailed information about which probes could selectively bind other metal(II) ion pairs would be challenging by simple inspection of their univariate spectroscopic response alone. Therefore, a large data set was collected on a series of main-group and d-block acetate and chloride salts; measurements were acquired at multiple wavelengths, and then pattern recognition techniques were used to interpret the data. Detailed information was obtained about which of these coumarin−enamine probes were most important for differentiation of ion pairs. We used fluorescent chemodosimeters **4**−**7** to discriminate seven divalent metal(II) ions, as chloride or acetate salts, using LDA for data interpretation. Somewhat surprisingly, in our previous communication using these fluorophores, probe **6** had been found to significantly contribute to the discrimination of metal chlorides, even though its *p*-pyridinyl nitrogen atom is the furthest from the metal-binding site (see the Sensor Design, Synthesis, and Characterization section) in this family of fluorophore compounds. This result ran counter to our working assumption at the time, i.e., that an accessible aromatic nitrogen atom would contribute favorably to metal coordination and, thus, better differential optical responses.

https://doi.org/10.1021/acs.inorgchem.1c01734
Inorg. Chem. 2021, 60, 14238−14252

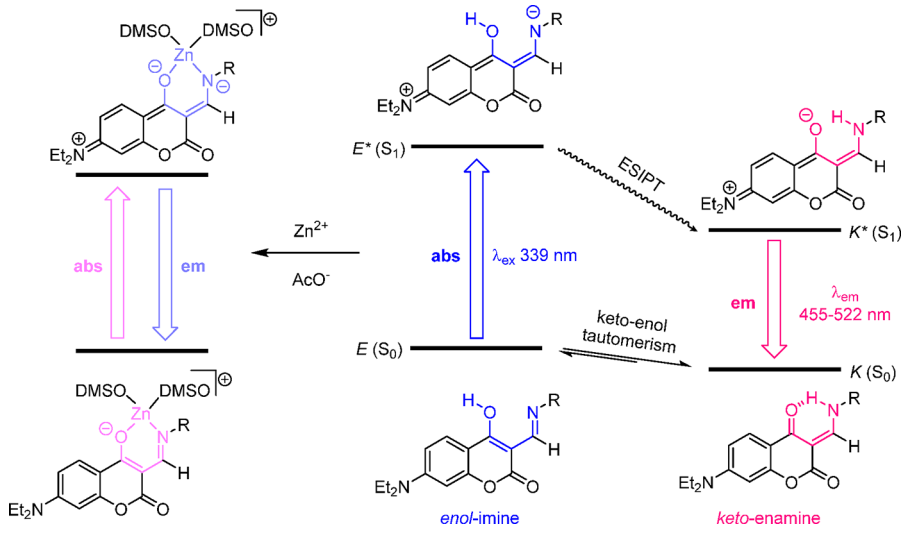

Figure 10. Energy diagram summarizing the proposed structures and relative energies of the electronic states responsible for photophysical processes in probes **3**–**7**. Highlighted are the ESIPT and keto–enol tautomerism. Coordination of metal ions such as zinc(II) induces deprotonation of the ligand and inhibits the ESIPT, so a new emission band corresponding to the bound enol complex is observed, with a concomitant CHEF.

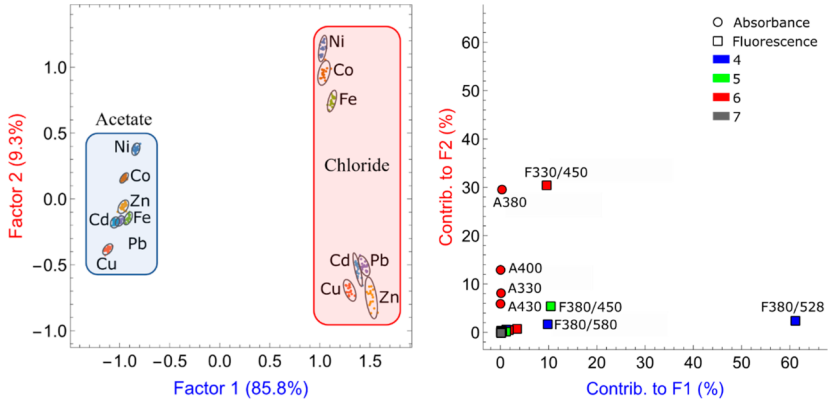

Figure 11. (Left) 2D plot of LDA scores depicting the separation of 14 divalent metal salts (2+ oxidation states), highlighting the separation along *factor 1* between acetate (blue) and chloride (red) metal salts. (Right) Corresponding LDA loading plots displaying the most important instrumental measurements to the first two factors: circles indicate absorbance measurements and squares fluorescence measurements.

However, the results of binding titrations of metals to probes **3** and **7**, presented here in the optical spectroscopy section, disproved that hypothesis. In fact, probe **3**, which contains no nitrogen atoms in its aromatic pendant ring, showed a metal-ion binding affinity comparable to probe **7**, one of whose two equivalent *o*-pyrimidinyl nitrogen atoms must always be near the metal-binding site. Therefore, we must conclude that pyridinyl nitrogen atoms in the vicinity of the metal-binding site *do not* contribute to the metal center's binding environment to any appreciable degree; on the contrary, they may even appear deleterious to the binding affinity and ion-pair discrimination, in accordance with the binding models proposed in this work. We also noted that the metal's counterion not only dramatically influences the affinity of the ligand for a given metal, but it also causes vast differences in the binding modes (bidentate vs monodentate).

To the best of our knowledge, using chemometrics methods to investigate ion pairs simultaneously has only been reported twice.[54,55] Can our previously reported discrimination results be improved upon by leveraging the counterion's influence, in light of the structural insights gained above? The results of analysis of the multivariate spectral data, detailed below, unearthed the sources of the trends mentioned above and helped to understand these probes' interactions with metal ions, particularly when paired with changes in the basicity of the metal's counteranion. They confirmed that a change in the counterions resulted in different degrees of deprotonation of the ligands' NH bond participating in the RAHB (Figure 2), modulating the metal binding affinity in response to the whole ion pair rather than to the nature of the metal cation alone. For instance, a higher degree of deprotonation of this position using a more basic counteranion improved the metal-ion binding affinity (see the NMR discussion). As a result, these chemodosimeters functioned as an effective dual-probe sensor for ion pairs, i.e., particular pairings of metal ions and specific counterions.

We chose to compare metal ions as their chloride and acetate salts to represent counterions with very different basicities. Seven divalent transition- and main-group-metal acetate salts [nickel(II), cobalt(II), iron(II), lead(II), zinc(II), cadmium(II), and copper(II)] were added to a 384-well microplate containing fluorescent probes **4**–**7**. All conditions were kept constant throughout, with [dye] = 16 μM and [metal salt] = 48 μM (3:1 salt/dye), dissolved in dry DMSO.

https://doi.org/10.1021/acs.inorgchem.1c01734
Inorg. Chem. 2021, 60, 14238–14252

For each sample, the absorbance was measured at five wavelengths (330, 380, 400, 430, and 600 nm); fluorescence emission at six wavelength pairs ($\lambda_{exc}/\lambda_{em}$ = 330/450, 330/528, 330/580, 380/450, 380/528, and 380/580 nm), i.e., in the spectral regions displaying the most significant changes upon the addition of metal salts to these probes (Figures S53 and S54).

The data obtained for the chloride and acetate metal salts exposed to compounds **4**−**7** were combined and subjected to LDA to find linear combinations of the above instrumental measurements that highlight the differences in the optical spectroscopic responses from chemodosimeters **4**−**7** to these ion pairs,[56] allowing for a more straightforward interpretation of the underlying chemical features responsible for these probes' responses to ion pairs. After LDA was carried out, the data set was represented by multidimensional descriptor variables (LDA factors, *F*), which, crucially, are returned by the algorithm in decreasing order of their information content. This allows for the straightforward dimensionality reduction of the original data set by retaining only the first two or three factors. The result is a 2D or three-dimensional data set, respectively, in which each observation is represented by a pair or a triplet of numbers (its *factor scores*). A graphical representation of these results for the probes' interaction with metal acetates or chlorides is displayed in Figure 11 as a 2D plot (an LDA *scores plot*). The most striking result is a clear separation between the chloride and acetate salts; indeed, the difference in behavior between acetate and chloride salts was more pronounced than the difference induced by the metal ions' identity, allowing us to clearly identify acetate versus chloride "superclusters" in the scores plot. This result, which may appear surprising at first, is in line with our previous conclusions regarding the possible role of anions as bases in modulating the emission properties of the ligands and complexes (e.g., by favoring the ESIPT vs CHEF mechanisms). In these results, differences along factor 1 (the horizontal axis in the scores plot) report on the nature of the anionic counterion in the ion pair; on the other hand, differences along factor 2 (the vertical axis) are linked with different cations.

It is interesting to investigate the source of these distinct and orthogonal discrimination behaviors. We can do so by examining the makeup of each LDA factor in terms of the original measurements: this is expressed by the LDA *factor loadings*, which are displayed graphically in a *loadings plot* in Figure 11. As an example, the loadings plot in Figure 11 indicates that the source of the differences among ion-pair samples seen along factor 1 is associated mainly with the differences in those samples' fluorescence emission at 528 nm when exposed to probe **4** (λ_{ex} = 380 nm). In general, the factor loadings provided valuable information about which chemodosimeters (**4**−**7**) and which types of measurement (absorbance vs fluorescence) were most important in discriminating among different anions and cations in each ion pair. In fact, the loadings plot indicated a greater contribution of fluorescence measurements linked with probes **4** and **5** to factor 1, i.e., the factor responsible for anion separation. On the other hand, to differentiate among metal cations, the system relied on differences in absorbance upon interaction of these ion pairs with probe **6**, which were found to be the most important contributors to factor 2. This was in agreement with the results we reported previously in which probe **6** was the strongest contributor to cation separation.[22]

Because we had found that probe **6** has slightly higher affinity for metal cations than the other probes, we conclude that the discrimination among metal cations is based mainly on their differences in affinity toward the coumarin−enamine family of ligands. Incidentally, this result further supports our amended binding hypothesis that having a pyridinyl nitrogen atom closer to the binding site is, in fact, a hindrance to metal-ion binding.

The binding affinity of these ligands for metal cations is significantly improved by the introduction of a basic counteranion. Indeed, probes **4** and **5**, which had not contributed much to the discrimination of metal chlorides in our previous study, gained much greater importance in the presence of the more basic acetate ion. Furthermore, in the current study, the separation among metal ions that had acetate as counteranion was much less pronounced than that among chloride salts likely because the acetate anion effectively increased all binding affinities; this, in turn, reduced the differences among metal ions, making their differentiation more challenging.

$NiCl_2$, $CoCl_2$, and $FeCl_2$ were well-separated from the other four metal chlorides ($PbCl_2$, $CdCl_2$, $ZnCl_2$, and $CuCl_2$) along factor 2, suggesting that the former three metal chlorides may themselves force deprotonation of the proton participating in RAHB (Figure 2) as a consequence of their stronger affinity to the ligand, whereas the latter four cations do not, leading to weaker binding. Differences in the binding mode can explain the distinctive discrimination between these two groups of metal(II) chloride salts. In fact, acetate is basic enough to deprotonate the fragment involved in RAHB to form the N^O$^-$ bidentate binding motif. The coumarin−enamine anion can then coordinate any of the metal ions with roughly comparable affinities (Table 3); this is reflected by the relative lack of discriminatory power among different metal ions (i.e., along factor 2 in the scores plot) when acetate is the counterion. On the other hand, the chloride supercluster contains two well-separated groups of metal cations, and, more in general, the separation among the cations is better with this counterion. This can be explained by assuming that the metal center initially binds in a monodentate fashion to either of the two different heteroatoms acting as possible ligands in the chemodosimeter. In fact, these coumarin−enamines contain both a hard Lewis basic site (oxygen atoms) and a borderline basic site (nitrogen atom). All of the metal(II) ions considered in this study are borderline Lewis acids except for cadmium(II), classified as a soft Lewis acid. However, nickel(II), cobalt(II), and iron(II), which behave similarly in these multivariate studies, have smaller atomic radii (approximately 70 pm) than cadmium(II), zinc(II), lead(II), and copper(II) (87, 88, 109, and 119 pm, respectively). HSAB theory suggests that the three smaller metal ions [nickel(II), cobalt(II), and iron(II)] will prefer to coordinate to the oxygen atom, the harder Lewis basic site; the other metal ions will have a higher affinity for the softer/borderline nitrogen atom. Additionally, monodentate binding to the nitrogen atom will inductively weaken the enol's OH bond: chloride may then be basic enough to deprotonate the enol to form the bidentate motif, liberating HCl and completing the coordination sphere.

We also found evidence to disprove the previously advanced hypothesis that an ortho nitrogen atom on the aromatic ring improves the metal binding affinity in this class of compounds. Indeed, studying probe **7**, whose pyrimidine (1,3-diazine) ring forces at least one nitrogen proximal to the metal binding site, showed that this was detrimental to differential metal binding

https://doi.org/10.1021/acs.inorgchem.1c01734
Inorg. Chem. 2021, 60, 14238−14252

and anion discrimination. We look forward to further studies to identify the role of the nitrogen atoms in the binding pocket, which could explain these experimental results more clearly, given their counterintuitive trend. The prominent role and differential responses of compounds **4**–**6** confirmed that these coumarin–enamine fluorophores can act as analytically useful dual-probe sensors for ion pairs.

3. CONCLUSION

In summary, we present an in-depth analysis of the metal binding behavior and corresponding structural and spectroscopic responses of a family of coumarin–enamine fluorescent probes as multiple-channel sensors. We identified multiple mechanisms responsible for the observed responses to main-group and transition-metal salts. The free probes experience ESIPT, leading to large Stokes shifts and low-energy emission, which is sensitive to the Brønsted and Lewis basicity of the metals' counteranions. Metal ions also inhibit the ESIPT mechanism, which is replaced by either CHEF, e.g., for zinc(II) and cadmium(II), or quenching by photoinduced electron transfer for other metal ions. Multivariate analysis of the spectral data highlighted the structural features of the chemodosimeters **4**–**7** responsible for their sensitivity to each class of analyte (i.e., anion vs cation). These results suggested that the degree of deprotonation of the RAHB motif by the counteranion was responsible for modulation of the affinity of these ligands toward the accompanying metal cations, resulting in a system that is sensitive not only to the nature of the metal cation but also to its counteranion, making it a sensor for ion pairs.

4. EXPERIMENTAL PROCEDURE

General Procedure for the [Zn(X)$_2$] Complex (X = Probe 3 or 7). The synthesis and full characterization for molecular probes **3**–**7** have previously been published.[22,40]

Either probe **3** or **7** (0.45 mmol) was dissolved in hot MeOH (10 mL), then Zn(OAc)$_2$ (0.22 mmol) was added to the solution, and the reaction was refluxed for 3 h. The solution was allowed to cool, forming a yellow precipitate. The solid was filtered and washed with cold MeOH. The yields for [Zn(**7**)$_2$] and [Zn(**3**)$_2$] were 85.9 mg (0.19 mmol, 52%) and 100.2 mg (0.14 mmol, 63%), respectively. 1D and 2D NMR spectra, IR spectra, and X-ray tables for [Zn(**3**)$_2$] are reported in the Supporting Information. HRMS-ESI for [Zn(**3**)$_2$]. Calcd for $[C_{40}H_{39}N_4O_6Zn]^+$ ([M + H]$^+$): *m*/*z* 735.2161. Found: *m*/*z* 735.2162. HRMS-ESI for [Zn(**7**)$_2$]. Calcd for $[C_{36}H_{35}N_8O_6Zn]^+$ ([M + H]$^+$): *m*/*z* 739.1971. Found: *m*/*z* 739.1977. Calcd for $[C_{36}H_{34}N_8O_6Zn + Na]^+$ ([M + Na]$^+$): *m*/*z* 761.1791. Found: *m*/*z* 761.1778.

■ ASSOCIATED CONTENT

Supporting Information

The Supporting Information is available free of charge at https://pubs.acs.org/doi/10.1021/acs.inorgchem.1c01734.

Experimental details and full characterization data including 1D and 2D NMR, IR, and mass spectrometry data and NMR, UV–vis, and fluorescence titration data, description of the statistical explanation used for the multivariate analysis, and X-ray crystallographic data (PDF)

Accession Codes

CCDC 2080861–2080864 and 2080948 contain the supplementary crystallographic data for this paper. These data can be obtained free of charge via www.ccdc.cam.ac.uk/data_request/cif, or by emailing data_request@ccdc.cam.ac.uk, or by contacting The Cambridge Crystallographic Data Centre, 12 Union Road, Cambridge CB2 1EZ, UK; fax: +44 1223 336033.

■ AUTHOR INFORMATION

Corresponding Authors

Karl J. Wallace − *Department of Chemistry and Biochemistry, The University of Southern Mississippi, Hattiesburg, Mississippi 39406, United States;* orcid.org/0000-0003-4541-7523; Email: karl.wallace@usm.edu

Marco Bonizzoni − *Department of Chemistry and Biochemistry, The University of Alabama, Tuscaloosa, Alabama 35487-0336, United States; Alabama Water Institute, The University of Alabama, Tuscaloosa, Alabama 35487-0206, United States;* orcid.org/0000-0003-0155-5481; Email: marco.bonizzoni@ua.edu

Authors

Aaron B. Davis − *Department of Chemistry and Biochemistry, The University of Southern Mississippi, Hattiesburg, Mississippi 39406, United States;* orcid.org/0000-0002-4099-931X

Michael H. Ihde − *Department of Chemistry and Biochemistry, The University of Alabama, Tuscaloosa, Alabama 35487-0336, United States;* orcid.org/0000-0002-0144-5146

Alie M. Busenlehner − *Department of Chemistry and Biochemistry, The University of Alabama, Tuscaloosa, Alabama 35487-0336, United States*

Dana L. Davis − *Department of Chemistry and Biochemistry, The University of Southern Mississippi, Hattiesburg, Mississippi 39406, United States*

Rashid Mia − *Department of Chemistry and Biochemistry, The University of Southern Mississippi, Hattiesburg, Mississippi 39406, United States*

Jessica Panella − *Department of Chemistry and Biochemistry, The University of Southern Mississippi, Hattiesburg, Mississippi 39406, United States*

Frank R. Fronczek − *Department of Chemistry, Louisiana State University, Baton Rouge, Louisiana 70803, United States;* orcid.org/0000-0001-5544-2779

Complete contact information is available at: https://pubs.acs.org/10.1021/acs.inorgchem.1c01734

Notes

The authors declare no competing financial interest.

■ ACKNOWLEDGMENTS

K.J.W. thanks the NSF (Grants OCE-0963064 and CHE-0840390 for the "Acquisition of a cyber accessible 400 MHz NMR at the University of Southern Mississippi) for financial support. M.B. and M.H.I. acknowledge support from the NSF MRI program (Grants CHE-1919906 and CHE-1726812), the NSF EPSCoR program (Grant OIA-1632825), and the Alabama Water Institute.

■ REFERENCES

(1) Mako, T. L.; Racicot, J. M.; Levine, M. Supramolecular luminescent sensors. *Chem. Rev.* **2019**, *119* (1), 322–477.

(2) Yang, Y.; Zhao, Q.; Feng, W.; Li, F. Luminescent chemodosimeters for bioimaging. *Chem. Rev.* **2013**, *113* (1), 192–270.

(3) Wallace, K. J.; Johnson, A. D. G.; Jones, W. S.; Manandhar, E. Chemodosimeters and chemoreactands for sensing ferric ions. *Supramol. Chem.* **2018**, *30* (5−6), 353−383.
(4) Sun, X.; Anslyn, E. V. An auto-inductive cascade for the optical sensing of thiols in aqueous media: Application in the detection of a VX nerve agent mimic. *Angew. Chem., Int. Ed.* **2017**, *56* (32), 9522−9526.
(5) Xu, Y.; Sen, S.; Wu, Q.; Zhong, X.; Ewoldt, R. H.; Zimmerman, S. C. Base-triggered self-amplifying degradable polyurethanes with the ability to translate local stimulation to continuous long-range degradation. *Chem. Sci.* **2020**, *11* (12), 3326−3331.
(6) Mahmudov, K. T.; Pombeiro, A. J. L. Resonance-assisted hydrogen bonding as a driving force in synthesis and a synthon in the design of materials. *Chem. - Eur. J.* **2016**, *22* (46), 16356.
(7) Meisner, Q. J.; Younes, A. H.; Yuan, Z.; Sreenath, K.; Hurley, J. J. M.; Zhu, L. Excitation-dependent multiple fluorescence of a substituted 2-(2′-hydroxyphenyl) benzoxazole. *J. Phys. Chem. A* **2018**, *122* (47), 9209−9223.
(8) Henary, M. M.; Fahrni, C. J. Excited state intramolecular proton transfer and metal ion complexation of 2-(2′-hydroxyphenyl)-benzazoles in aqueous solution. *J. Phys. Chem. A* **2002**, *106* (21), 5210−5220.
(9) Liu, D.; Ding, Q.; Fu, Y.; Song, Z.; Peng, Y. Rh-catalyzed C−H amidation of 2-Arylbenzo [d] thiazoles: an approach to single organic molecule white light emitters in the solid state. *Org. Lett.* **2019**, *21* (8), 2523−2527.
(10) Philipova, T.; Ivanova, C.; Kamdzhilov, Y.; Teresa Molina, M. Deprotonation and protonation studies of some substituted 1,4- and 9,10-anthraquinones. *Dyes Pigm.* **2002**, *53*, 219−227.
(11) Mohammed, O. F.; Xiao, D.; Batista, V. S.; Nibbering, E. T. J. Excited-state intramolecular hydrogen transfer (ESIHT) of 1, 8-Dihydroxy-9, 10-anthraquinone (DHAQ) characterized by ultrafast electronic and vibrational spectroscopy and computational modeling. *J. Phys. Chem. A* **2014**, *118* (17), 3090−3099.
(12) Nagaoka, S.-I.; Endo, H.; Ohara, K.; Nagashima, U. Correlation between excited-state intramolecular proton-transfer and singlet-oxygen quenching activities in 1-(acylamino) anthraquinones. *J. Phys. Chem. B* **2015**, *119* (6), 2525−2532.
(13) Ghosh, D.; Ahamed, G.; Batuta, S.; Begum, N. A.; Mandal, D. 30,40-methylenedioxy-3-hydroxyflavone: switchover from reversible to irreversible ESIPT along the n-alcohol series. *J. Photochem. Photobiol., A* **2016**, *328*, 77−86.
(14) Karmakar, A.; Mallick, T.; Fouzder, C.; Mukhuty, A.; Mondal, S.; Pramanik, A.; Kundu, R.; Mandal, D.; Begum, N. A. Unfolding the role of a flavone-based fluorescent antioxidant towards the misfolding of amyloid proteins: An endeavour to probe amyloid aggregation. *J. Phys. Chem. B* **2020**, *124* (49), 11133−11144.
(15) Chumak, A. Y.; Mudrak, V. O.; Kotlyar, V. M.; Doroshenko, A. O. 4′-Nitroflavonol fluorescence: Excited state intramolecular proton transfer reaction from the non-emissive excited state. *J. Photochem. Photobiol., A* **2021**, *406*, 112978.
(16) Kwon, J. E.; Park, S. Y. Advanced organic optoelectronic materials: Harnessing excited-state intramolecular proton transfer (ESIPT) process. *Adv. Mater.* **2011**, *23*, 3615−3642.
(17) You, L.; Zha, D.; Anslyn, E. V. Recent advances in supramolecular analytical chemistry using optical sensing. *Chem. Rev.* **2015**, *115* (15), 7840−7892.
(18) Pushina, M.; Farshbaf, S.; Shcherbakova, E. G.; Anzenbacher, P. A dual chromophore sensor for the detection of amines, diols, hydroxy acids, and amino alcohols. *Chem. Commun.* **2019**, *55* (31), 4495−4498.
(19) Ngernpimai, S.; Geng, Y.; Makabenta, J. M.; Landis, R. F.; Keshri, P.; Gupta, A.; Li, C.-H.; Chompoosor, A.; Rotello, V. M. Rapid identification of biofilms using a robust multichannel polymer sensor array. *ACS Appl. Mater. Interfaces* **2019**, *11* (12), 11202−11208.
(20) Kostereli, Z.; Severin, K. Array-based sensingof purine derivatives with fluorescent dyes. *Org. Biomol. Chem.* **2015**, *13*, 9231−9235.
(21) Li, Z.; Suslick, K. S. Portable optoelectronic nose for monitoring meat freshness. *ACS Sensors* **2016**, *1* (11), 1330−1335.
(22) Mallet, A. M.; Davis, A. B.; Davis, D. R.; Panella, J.; Wallace, K. J.; Bonizzoni, M. A cross reactive sensor array to probe divalent metal ions. *Chem. Commun.* **2015**, *51* (95), 16948−16951.
(23) Umali, A. P.; Anslyn, E. V. A general approach to differential sensing using synthetic molecular receptors. *Curr. Opin. Chem. Biol.* **2010**, *14*, 685−692.
(24) Sasaki, Y.; Minamiki, T.; Tokito, S.; Minami, T. A molecular self-assembled colourimetric chemosensor array for simultaneous detection of metal ions in water. *Chem. Commun.* **2017**, *53* (49), 6561−6564.
(25) He, W.; Luo, L.; Liu, Q.; Chen, Z. Colorimetric sensor array for discrimination of heavy metal ions in aqueous solution based on three kinds of thiols as receptors. *Anal. Chem.* **2018**, *90* (7), 4770−4775.
(26) Bowyer, A. A.; Shen, C.; New, E. J. A fluorescent three-sensor array for heavy metals in environmental water sources. *Analyst* **2020**, *145* (4), 1195−1201.
(27) Xu, Y.; Bonizzoni, M. Disposable paper strips for carboxylate discrimination. *Analyst* **2020**, *145* (10), 3505−3516.
(28) Tropp, J.; Ihde, M. H.; Williams, A. K.; White, N. J.; Eedugurala, N.; Bell, N. C.; Azoulay, J. D.; Bonizzoni, M. A sensor array for the discrimination of polycyclic aromatic hydrocarbons using conjugated polymers and the inner filter effect. *Chem. Sci.* **2019**, *10* (44), 10247−10255.
(29) Wang, B.; Han, J.; Bojanowski, N. M.; Bender, M.; Ma, C.; Seehafer, K.; Herrmann, A.; Bunz, U. H. An optimized sensor array identifies all natural amino acids. *ACS sensors* **2018**, *3* (8), 1562−1568.
(30) Mallet, A. M.; Liu, Y.; Bonizzoni, M. An off-the-shelf sensing system for physiological phosphates. *Chem. Commun.* **2014**, *50* (39), 5003−5006.
(31) Pezzato, C.; Lee, B.; Severin, K.; Prins, L. J. Pattern-based sensing of nucleotides with functionalized gold nanoparticles. *Chem. Commun.* **2013**, *49* (5), 469−471.
(32) Pode, Z.; Peri-Naor, R.; Georgeson, J. M.; Ilani, T.; Kiss, V.; Unger, T.; Markus, B.; Barr, H. M.; Motiei, L.; Margulies, D. Protein recognition by a pattern-generating fluorescent molecular probe. *Nat. Nanotechnol.* **2017**, *12* (12), 1161−1168.
(33) Mao, J.; Lu, Y.; Chang, N.; Yang, J.; Zhang, S.; Liu, Y. Multidimensional colorimetric sensor array for discrimination of proteins. *Biosens. Bioelectron.* **2016**, *86*, 56−61.
(34) Hatai, J.; Motiei, L.; Margulies, D. Analyzing amyloid beta aggregates with a combinatorial fluorescent molecular sensor. *J. Am. Chem. Soc.* **2017**, *139* (6), 2136−2139.
(35) Zamora-Olivares, D.; Kaoud, T. S.; Zeng, L.; Pridgen, J. R.; Zhuang, D. L.; Ekpo, Y. E.; Nye, J. R.; Telles, M.; Anslyn, E. V.; Dalby, K. N. Quantification of ERK kinase activity in biological samples using differential sensing. *ACS Chem. Biol.* **2020**, *15* (1), 83−92.
(36) Abeywickrama, C. S.; Pang, Y. Synthesis of fused 2-(2′-Hydroxyphenyl)benzoxazole derivatives: The impact of meta-/para-substitution on fluorescence and zinc binding. *Tetrahedron Lett.* **2016**, *57*, 3518−3522.
(37) Henary, M. M.; Wu, Y.; Fahrni, C. J. Zinc(II)-selective ratiometric fluorescent sensors based on inhibition of excited-state intramolecular proton transfer. *Chem. - Eur. J.* **2004**, *10* (12), 3015−25.
(38) Wallace, K. J.; Fagbemi, R. I.; Folmer-Andersen, F. J.; Morey, J.; Lynth, V. M.; Anslyn, E. V. Detection of chemical warfare simulants by phosphorylation of a coumarin oximate. *Chem. Commun.* **2006**, 3886−3888.
(39) Hettie, K. S.; Glass, T. E. Coumarin-3-Aldehyde as a Scaffold for the Design of Tunable PET-Modulated Fluorescent Sensors for Neurotransmitters. *Chem. - Eur. J.* **2014**, *20*, 17488−17499.
(40) Davis, A. B.; Lambert, R. E.; Fronczek, F. R.; Cragg, P. J.; Wallace, K. J. An activated coumarin-enamine Michael acceptor for CN^-. *New J. Chem.* **2014**, *38* (10), 4678−4683.

https://doi.org/10.1021/acs.inorgchem.1c01734
Inorg. Chem. 2021, 60, 14238−14252

(41) Loots, L.; Barbour, L. J. A simple and robust method for the identification of pi-pi packing motifs of aromatic compounds. *CrystEngComm* **2012**, *14*, 300−304.
(42) Cotton, F. A.; Wilkinson, G.; Murillo, C. A.; Bochmann, M.; Grimes, R. *Advanced inorganic chemistry*; Wiley: New York, 1988; Vol. *6*.
(43) Hancock, R. D.; Martell, A. E. Ligand design for selective complexation of metal ions in aqueous solution. *Chem. Rev.* **1989**, *89*, 1875−1914.
(44) Benisvy, L.; Bill, E.; Blake, A. J.; Collison, D.; Davies, E. S.; Garner, C. D.; McArdle, G.; McInnes, E. J.; McMaster, J.; Ross, S. H.; Wilson, C. Phenoxyl radicals: H-bonded and coordinated to Cu(II) and Zn(II). *Dalton Trans.* **2006**, *1*, 258−267.
(45) Tong, Y. P.; Zheng, S. L.; Chen, X. M. Structures, Photoluminescence and Theoretical Studies of Two ZnII Complexes with Substituted 2-(2-Hydroxyphenyl) benzimidazoles. *Eur. J. Inorg. Chem.* **2005**, *2005* (18), 3734−3741.
(46) Zhou, Z.; Li, W.; Hao, X.; Redshaw, C.; Chen, L.; Sun, W.-H. 6-Benzhydryl-4-methyl-2-(1H-benzoimidazol-2-yl) phenol ligands and their zinc complexes: Syntheses, characterization and photoluminescence behavior. *Inorg. Chim. Acta* **2012**, *392*, 345−353.
(47) Kolthoff, I. M.; Chantooni, M. K., Jr; Bhowmik, S. Dissociation constants of uncharged and monovalent cation acids in dimethyl sulfoxide. *J. Am. Chem. Soc.* **1968**, *90* (1), 23−28.
(48) Bordwell, F. G. Equilibrium acidities in dimethyl sulfoxide solution. *Acc. Chem. Res.* **1988**, *21* (12), 456−463.
(49) Davis, B. D.; Fronczek, F. R.; Wallace, K. J. Crystal structure of diaquabis(7-diethylamino-3-formyl-2-oxo-2*H*-chromen-4-olato-k^2O^3,O^4)-zinc(II) dimethyl sulfoxide disolvate. *Acta Crystallogr.* **2016**, *72*, 1032−1036.
(50) Davis, A. B. A library of coumarin enamine chemodosimeters for the detection of analytes Dissertation. Thesis, The University of Southern Mississippi, Hattiesburg, MS, 2016.
(51) Cheng, Y.-M.; Pu, S.-C.; Yu, Y.-C.; Chou, P.-T.; Huang, C.-H.; Chen, C.-T.; Li, T.-H.; Hu, W.-P. Spectroscopy and Femtosecond Dynamics of 7-N,N-Diethylamino-3-hydroxyflavone. The Correlation of Dipole Moments among Various States To Rationalize the Excited-State Proton Transfer Reaction. *J. Phys. Chem. A* **2005**, *109*, 11696.
(52) Gans, P. *HypSpec*; Protonic Software: Leeds, U.K., 2014.
(53) Sedgwick, A. C.; Wu, L.; Han, H.-H.; Bull, S. D.; He, X.-P.; James, T. D.; Sessler, J. L.; Tang, B. Z.; Tian, H.; Yoon, J. Excited-state intramolecular proton-transfer (ESIPT) based fluorescence sensors and imaging agents. *Chem. Soc. Rev.* **2018**, *47* (23), 8842−8880.
(54) García-Acosta, B.; Martínez-Máñez, R.; Sancenón, F.; Soto, J.; Rurack, K.; Spieles, M.; García-Breijo, E.; Gil, L. Ditopic N-crowned 4-(p-aminophenyl)-2, 6-diphenylpyridines: Implications of macrocycle topology on the spectroscopic properties, cation complexation, and differential anion responses. *Inorg. Chem.* **2007**, *46* (8), 3123−3135.
(55) Lei, C.; Dai, H.; Fu, Y.; Ying, Y.; Li, Y. Colorimetric sensor array for thiols discrimination based on urease−metal ion pairs. *Anal. Chem.* **2016**, *88* (17), 8542−8547.
(56) Brereton, R. G. *Chemometrics: Data Driven Extraction for Science*, 2nd ed.; Wiley Interscience: Chichester, U.K., 2018.

https://doi.org/10.1021/acs.inorgchem.1c01734
Inorg. Chem. 2021, 60, 14238−14252